Dynamical properties of the magnetic topological insulator $T\mathrm{Bi_2Te_4}$ (T=Mn, Fe): Phonons dispersion, Raman active modes, and chiral phonons study

Aksel Kobiałka [1,2,*], Małgorzata Sternik [3,†] and Andrzej Ptok [3,‡]

[1] *Institute of Physics, Maria Curie-Skłodowska University, Plac Marii Skłodowskiej-Curie 1, PL-20031 Lublin, Poland*

[2] *Department of Physics, University of Basel, Klingelbergstrasse 82, CH-4056 Basel, Switzerland*

[3] *Institute of Nuclear Physics, Polish Academy of Sciences, W. E. Radzikowskiego 152, PL-31342 Kraków, Poland*

(Received 1 February 2022; accepted 1 June 2022; published 14 June 2022)

Recently discovered magnetic topological insulators $T\mathrm{Bi_2Te_4}$ (T = Mn, Fe) crystallize into the $R\bar{3}m$ rhombohedral structure and exhibit the antiferromagnetic order. Here, we discuss the lattice dynamics of these compounds to confirm the stability of these systems. We show that the phonon dispersion does not contain soft modes, so both compounds are dynamically stable in the $R\bar{3}m$ phase. We perform theoretical analyses of the mode activity at the Γ point for the discussed compounds. In the case of the Raman active modes, our results are in agreement with the experimentally observed frequencies. Finally, we also discuss the possibility of the realization of chiral phonons.

DOI: 10.1103/PhysRevB.105.214304

I. INTRODUCTION

$\mathrm{MnBi_2Te_4}$ is the first intrinsic antiferromagnetic (AFM) topological insulator [1,2] that has been recently observed experimentally. Similarly to the other topological insulators (TI), this system possesses a layered structure (Fig. 1), while layers are bonded by the van der Waals interaction. Below $T_\mathrm{N} = 25$ K, the A-type AFM order with opposite spin orientations in two adjacent ferromagnetic Mn layers is realized [3–5]. An interplay between the topological properties of this system and the intrinsic magnetic order allows for the realization of many quantum phenomena including the quantum anomalous Hall effect [6,7] or axion insulator state [8].

The topological properties of the $\mathrm{MnBi_2Te_4}$ are exhibited by the realization of the electronic surface states [9–13], which in similarity to the case of TI ($\mathrm{Bi_2Se_3}$ or $\mathrm{Bi_2Te_3}$), form Dirac cones. However, contrary to the ordinary TI, due to the intrinsic magnetic order, the time-reversal symmetry breaking occurs and the Dirac gap is observed in the surface states [14–16]. Nevertheless, these surface states can give a dominant contribution to the electron–phonon interaction [17–19].

More recently, a successful single crystal growth of $\mathrm{FeBi_2Te_4}$ was reported [20]. The structure of this compound and its physical characteristics are not yet confirmed in a theoretical study, but it seems to have topological properties similar to the $\mathrm{MnBi_2Te_4}$. In this paper, we present the theoretical study of the structure and lattice dynamics performed for both compounds, $\mathrm{MnBi_2Te_4}$ and $\mathrm{FeBi_2Te_4}$. We confirm the dynamical stability of both crystals and the consistency between calculated and measured data on both structural parameters and their Raman shifts. Moreover, we calculate the circular polarization of Te and Bi atoms and demonstrate that the emergence of chiral modes in these materials is feasible.

The paper is organized as follows. First, we briefly describe the computational details (Sec. II). The phonon dispersions are presented and discussed in Sec. III. Next, in Sec. IV, we discuss thoroughly the Raman-active modes in relation to the available experimental and theoretical results. In Sec. V, we discuss the realization of the chiral phonons in the $T\mathrm{Bi_2Te_4}$. Finally, we conclude our findings in Sec. VI.

II. CALCULATION DETAILS

The first-principles density functional theory (DFT) calculations were performed using the projector augmented-wave (PAW) potentials [21] implemented in the Vienna *ab initio* Simulation Package (VASP) code [22–24]. The calculations are made within the generalized gradient approximation (GGA) in the Perdew, Burke, and Ernzerhof (PBE) parametrization [25]. Strong local electron interaction on the 3*d* orbitals of transition metals were taken into account using DFT + U scheme [26], with the intraorbital Coulomb parameter U = 5.0 eV, similarly to the earlier studies [27]. Additionally, we included the spin-orbit coupling (SOC) as well as the van der Waals (vdW) corrections within the Grimme scheme (DFT-D2) [28].

The magnetic unit cells (i.e., cells presented in Fig. 1 with A-type AFM order) were optimized using $24 \times 24 \times 4$ **k**-point Γ-centered grids in the Monkhorst-Pack scheme [29]. The energy cutoff for the plane-wave expansion is set to 450 eV. The condition for the breaking of the optimization loop was the energy difference of 10^{-6} eV and 10^{-8} eV for ionic and electronic degrees of freedom for subsequent steps. The crystal symmetry was analyzed using FINDSYM [30] and SPGLIB [31], while the momentum space analysis was done using SEEK-PATH tools [32].

*akob@kft.umcs.lublin.pl
†sternik@wolf.ifj.edu.pl
‡aptok@mmj.pl

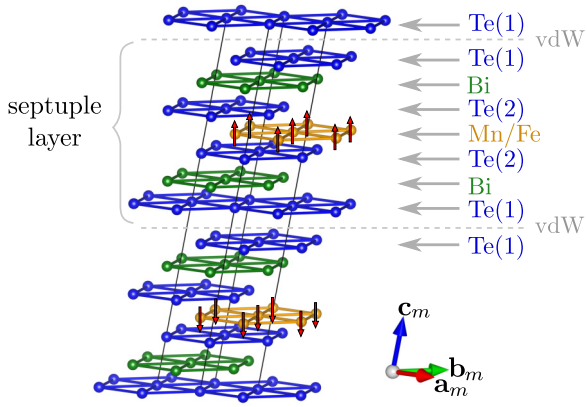

FIG. 1. The unit cell of magnetic topological insulator $T\mathrm{Bi_2Te_4}$ (T = Mn, Fe) with the A-type antiferromagnetic order.

The dynamical properties were calculated using the direct *Parlinski-Li-Kawazoe* method [33]. Under this calculation, the interatomic force constants (IFC) are found from the forces acting on atoms when an individual atom is displaced. The forces were obtained by the first-principle calculations with VASP using the supercell containing $3 \times 3 \times 1$ magnetic unit cells and reduced Γ-centered $3 \times 3 \times 2$ $\boldsymbol{k}$ mesh. The phonon dispersion and polarization vectors analyses were performed using the ALAMODE software [34]. The mode symmetries at the Γ point were found by the PHONON software [35].

III. LATTICE DYNAMICS

A. Crystal structure

$T\mathrm{Bi_2Te_4}$ crystallizes in the trigonal $R\bar{3}m$ (space group 166) lattice with one chemical formula in the primitive unit cell or three formula units in the conventional unit cell. The system is composed of septuple layer (SL) slabs [containing the sequence of Te(1)–Bi–Te(2)–(Mn/Fe)–Te(2)–Bi–Te(1) monoatomic layers], separated by the vdW gaps appearing between two adjacent Te(1) layers (Fig. 1). The lattice parameters found experimentally are $a = 4.29$ Å and $c = 41.67$ Å for $\mathrm{MnBi_2Te_4}$ [36] and $a = 4.26$ Å and $c = 41.46$ Å for $\mathrm{FeBi_2Te_4}$ [20]. In our calculations, we use the A-type antiferromagnetic unit cell (shown in Fig. 1), which is built from two primitive unit cells and contains two transition metal layers. In this supercell, all symmetry elements of $R\bar{3}m$ space group remain unchanged. The relaxed magnetic unit cells are described by $a_m = b_m = 4.29$ (4.26) Å, $c_m = 28.22$ (28.07) Å, $\alpha = 90^\circ$, $\beta = 81.25^\circ$ (81.27°), and $\gamma = 120^\circ$ for compound with Mn (Fe) atoms. The obtained parameters correspond to the hexagonal lattice with $a = 4.29$ Å, and $c = 41.67$ Å for $\mathrm{MnBi_2Te_4}$, and $a = 4.26$ Å, and $c = 41.46$ Å for $\mathrm{FeBi_2Te_4}$. Our theoretical findings are in excellent agreement with the experimental results. The Bi, Te(1), Te(2), and T=Mn, Fe atoms are located in Wyckoff positions 6c (0,0,z_{Bi}), 6c (0,0,$z_{\mathrm{Te(1)}}$), 6c (0,0,$z_{\mathrm{Te(2)}}$), and 3c (0,0,0), respectively. We find $z_{\mathrm{Bi}} = 0.42$, $z_{\mathrm{Te(1)}} = 0.13$, and $z_{\mathrm{Te(2)}} = 0.29$ for both compounds.

B. Lattice dynamics calculations

Lattice vibrations, called phonons, are charge neutral and spinless elementary excitations, contrary to the electrons which are charged and spinfull particles [37]. Therefore, the approach to the electron and phonon band structure calculations can be different. In the case of electron structure, the magnetic atoms with opposite spins have to be distinguished, which can lead to the enlargement of unit cell. For $T\mathrm{Bi_2Te_4}$, the realization of the A-type AFM order involves the use of the magnetic unit cell which is doubled with respect to the primitive one.

By contrast, phonons do not directly interact with magnetic moments of atoms. The assumed magnetic order have an impact on the phonon spectrum by the changes in the interatomic force constants induced by the different magnetic arrangements. During these calculations the supercell with A-type AFM order is utilized, but then the phonon dispersion relations are calculated using the basic primitive unit cell. We applied this standard method in phonon calculations of $T\mathrm{Bi_2Te_4}$. Nevertheless, when the strong spin-phonon coupling is expected, the enlarged primitive unit cell (with "spin-recognized" magnetic atoms) should be taken into account [38].

To examine the compatibility of both methods, we performed the phonon calculations using the magnetic unit cell (doubly enlarged and containing two formula units). The details of these calculations and resulted phonon dispersion curves, characteristic frequencies, and symmetries of the modes at the Γ point and phonon densities of states are presented in the Supplemental Material (SM) [39].

C. Phonon dispersion

The phonon dispersions of $T\mathrm{Bi_2Se_4}$ calculated using the basic primitive unit cell are presented in Fig. 2. The introduction of the spin-orbit interaction in the calculations does not change the phonon dispersion qualitatively. In the phonon dispersion, all acoustic branches show a linear dispersion in the vicinity of the Γ point. No imaginary phonon frequency was found for any system, which indicates the stability of these systems in the $R\bar{3}m$ phase. For this reason, we can expect that the small substitution of Fe should be possible for the base system $\mathrm{MnBi_2Se_4}$, contrary to the hole doping by Ca or Mg, which leads to substantial instability in the recently studied systems [40]. Similar results were obtained in calculations performed using the magnetic unit cell (containing two formula units with 14 atoms) that corresponds to the 42 modes. There are no imaginary frequencies in the calculated phonon branches presented in Fig. S1 in SM [39].

D. Phonon density of states

The total and partial density of states are presented in Fig. 3. As we can see, the vibrational modes of heavy Bi contribute mainly to the low range of frequencies. Vibrations of Te in the first and second positions [i.e., Te(1) and Te(2)] are placed in two separated frequency areas at the middle frequency region between T =(Mn,Fe) and Bi atomic layers. The Te(1) atoms, which create a two-layer-like structure, separated by the vdW gap (see Fig. 1), vibrate with higher

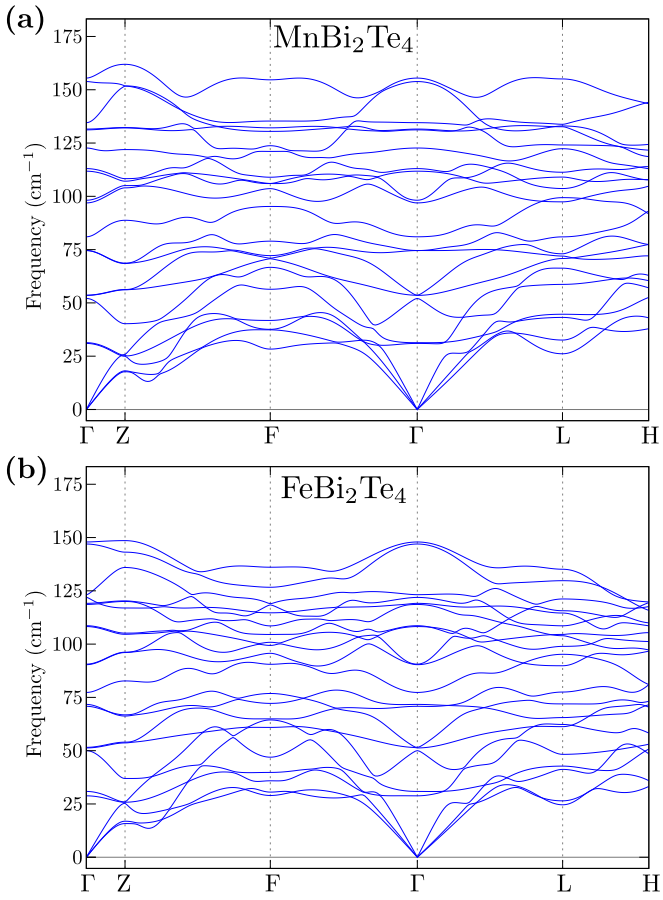

FIG. 2. The phonon dispersion along high symmetry directions.

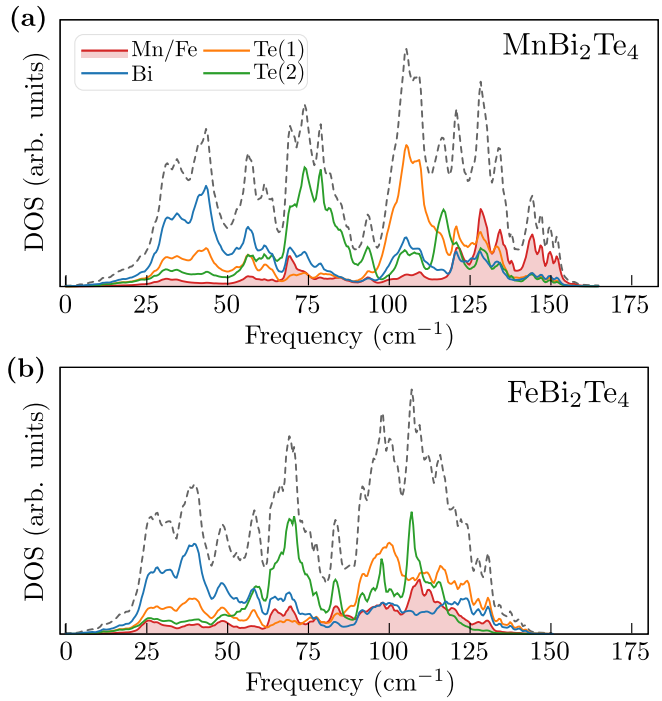

FIG. 3. The total (dashed line) and partial (solid lines) phonon density of states.

TABLE I. Characteristic frequencies in cm^{-1}, activities (R – Raman, IR – infrared) and symmetries of the modes at the Γ point.

	$MnBi_2Te_4$			$FeBi_2Te_4$	
Freq.	Activity	Symm.	Freq.	Activity	Symm.
30.65	R	E_g	29.35	R	E_g
51.20	R	A_{1g}	49.17	R	A_{1g}
52.67	IR	E_u	50.60	IR	E_u
73.32	R	E_g	70.05	R	E_g
76.66	IR	A_{2u}	76.02	IR	A_{2u}
95.90	IR	E_u	88.93	IR	E_u
110.51	R	E_g	106.57	R	E_g
120.58	R	A_{1g}	116.92	IR	E_u
129.16	IR	E_u	119.82	R	A_{1g}
132.23	IR	A_{2u}	121.05	IR	A_{2u}
151.21	R	A_{1g}	144.23	IR	A_{2u}
152.84	IR	A_{2u}	145.37	R	A_{1g}

frequencies (around 100 cm^{-1}) than the Te(2) atoms that oscillate with average frequency of 75 cm^{-1}. Finally, T = (Mn,Fe) modes are located in the range of high frequencies. Interestingly, for both systems, the phonon dispersion associated with these modes creates a flat band around 130 cm^{-1} or 120 cm^{-1} in Mn or Fe compounds, respectively (see Fig. 2).

IV. RAMAN ACTIVE MODES

A. Irreducible representations

The phonon modes of TBi_2Te_4 at the Γ point can be decomposed into the irreducible representations of the space group $R\bar{3}m$ as follows:

$$\Gamma_{\text{acoustic}} = A_{2u} + E_u,$$
$$\Gamma_{\text{optic}} = 3A_{1g} + 3A_{2u} + 3E_u + 3E_g.$$

In total, there are 21 vibrational modes, seven nondegenerate A_{1g} and A_{2u} modes, and seven doubly degenerate E_u and E_g modes. Here, optical vibrations $3A_{2u} + 3E_u$ are infrared active (IR), while optical modes $3A_{1g} + 3E_g$ are Raman (R) active. The activity and symmetries of the modes at Γ point for TBi_2Te_4 are presented in Table I.

The atoms participating in the vibrations of the E_g and E_u types oscillate in the SL plane (*a*-*b* plane in Fig. 1). Contrary to this, the modes A_{1g} and A_{2u} are related to out-of-plane oscillations (perpendicular to the *a*-*b* plane). Interestingly, the magnetic T atoms do not participate in the vibrations of the Raman active modes (i.e., A_{1g} and E_g).

B. Selection rules for Raman-active modes

The nonresonant Raman scattering intensity depends in general on the directions of the incident and scattered light relative to the principal axes of the crystal. It is expressed by Raman tensor R, relevant for a given crystal symmetry, as [41]

$$I \propto |e_i \cdot R \cdot e_s|^2, \quad (1)$$

where e_i and e_s are the polarization vectors of the incident and scattered light, respectively. According to the group theory,

TABLE II. Selection rules for Raman-active modes.

Configuration	A_{1g}	E_g
e_x in e_x out (linear ∥)	$\|a\|^2$	$\|c\|^2$
e_x in e_y out (linear ⊥)	0	$\|c\|^2$
σ^+ in σ^+ out (cocircular)	$\|a\|^2$	0
σ^+ in σ^- out (cross-circular)	0	$2\|c\|^2$

the Raman tensor for the $R\bar{3}m$ space group takes the following forms for the A_{1g} and E_g modes:

$$R(A_{1g}) = \begin{pmatrix} a & 0 & 0 \\ 0 & a & 0 \\ 0 & 0 & b \end{pmatrix} \quad \text{and}$$

$$R\left(E_g^{\mathrm{I}}\right) = \begin{pmatrix} c & 0 & 0 \\ 0 & -c & d \\ 0 & d & 0 \end{pmatrix}; \; R\left(E_g^{\mathrm{II}}\right) = \begin{pmatrix} 0 & -c & -d \\ -c & 0 & 0 \\ -d & 0 & 0 \end{pmatrix}. \tag{2}$$

In the backscattering configuration, e_i and e_s are placed within the xy plane. The polarization vectors for linearly polarized light in the x and y directions are $e_x = (1\,0\,0)$ and $e_y = (0\,1\,0)$, respectively. Similarly, the polarization vector for left σ^+ and right σ^- circularly polarized light are $\sigma^{\pm} = \frac{1}{\sqrt{2}}(1 \pm i\,0)$. Using Eq. (1) and the Raman tensors (2), we can determine the selection rules and Raman intensities for various scattering geometries. Table II summarizes the Raman response in the backscattering geometry for four polarization configurations. As we can see, it is possible to distinguish the A_{1g} and E_g using the different backscattering configurations. The same holds for both linear and circularly polarized Raman spectra measurements. For example, this property of the Raman modes was used to differentiate between Raman active modes using co- and cross-circular Raman back-scattering in Ref. [42]. The group theory study of the vibrational modes in bulk paramagnetic $T\mathrm{Bi_2Te_4}$, the phonon selection rules, and the real-space displacements corresponding to each mode are presented in Ref. [43].

C. Comparison with related results

In Table III, we present a comparison of our theoretically obtained frequencies of the Raman active modes with previous results (both experimental and theoretical). It should be mentioned that not all Raman modes can be observed at each measurement. This is caused by the relatively weak intensity of some Raman modes and the insensitivity of the used method for observing low-frequency modes. For example, for $\mathrm{MnBi_2Te_4}$, in Refs. [36,44] only four Raman frequencies are observed, while in Ref. [42] we can distinguish five distinctive peaks. Similarly, in the case of the $\mathrm{FeBi_2Te_4}$, the Raman spectroscopy experiment exhibits three distinct phonon modes at 65 $\mathrm{cm^{-1}}$, 110 $\mathrm{cm^{-1}}$, and 132 $\mathrm{cm^{-1}}$ along with two split secondary modes at 90 $\mathrm{cm^{-1}}$ and 144 $\mathrm{cm^{-1}}$ [20]. The measured frequencies are slightly lower than the values obtained in the calculations. The biggest difference of ∼12 $\mathrm{cm^{-1}}$ is observed for the high-frequency A_{1g} mode. The reason for that

TABLE III. Comparison of the Raman-active modes frequencies ($\mathrm{cm^{-1}}$) for different compounds.

E_g	A_{1g}	E_g	E_g	A_{1g}	A_{1g}		
				$\mathrm{MnBi_2Te_4}$			
30.65	51.20	73.32	110.51	120.58	151.21	**This work**	
—	46	65	102	—	138	Measurement	[36]
—	47.4	67.4	104.2	—	139.8	Measurement	[44]
—	45.7	66.9	103.4	113.5	138.6	Measurement	[42]
26.9	48.0	68.3	105.1	115.6	140.0	Measurement	[47]
—	47	60	105	—	142	Calculation	[36]
30.3	46.0	74.5	109.6	117.4	144.1	Calculation	[42]
29.4	51.8	73.4	109.1	119.4	149.1	Calculation	[47]
				$\mathrm{FeBi_2Te_4}$			
29.35	49.17	70.05	106.57	119.82	145.37	**This work**	
—	—	65	—	110	132	Measurement	[20]
				$\mathrm{Bi_2Te_3}$			
—	62.5	—	103	—	134	Measurement	[48]
—	61.5	—	101.5	—	133.5	Measurement	[49]
—	62.3	—	103	—	134	Measurement	[50]
34.4	62.1	—	101.7	—	134.0	Measurement	[51]
42.4	66.4	—	106.7	—	134.8	Calculation	[52]
42.1	64.2	—	112.3	—	139.2	Calculation	[49]
50.6	71.1	—	118.5	—	128.3	Calculation	[53]

can be the temperature at which the measurement is carried out. Recent experiments on $\mathrm{MnBi_2Te_4}$ show that the increase of temperature [42] leads to the shift of the Raman frequency modes to lower values. A similar temperature dependence of the Raman frequencies was observed for isostructural materials, $\mathrm{PbBi_2Te_4}$ [45] and $\mathrm{GeBi_2Te_4}$ [46]. In contrast, the external pressure imposed on the $\mathrm{MnBi_2Te_4}$ crystal causes the increase of mode frequencies [44]. Finally, we briefly describe the differences between the Raman frequencies in $T\mathrm{Bi_2Te_4}$ and in the parent $\mathrm{Bi_2Te_3}$ material. In the studied materials, the TTe layer is inserted in van der Waals gaps of $\mathrm{Bi_2Te_3}$ layers. Due to similar crystal structures described by the same space-group symmetry, the four Raman modes of $\mathrm{Bi_2Te_3}$ correspond to four Raman modes of $T\mathrm{Bi_2Te_4}$. The smaller number of Raman active modes is caused by the smaller number of atoms in the unit cell. The modifications of the crystal structure induced by additional TTe layers lead to the changes of distance and strength of the covalent bonds between pairs of atoms. This, in turn, results in the shift of Raman modes (cf. Table III).

For example, the frequency of the first A_{1g} mode is reduced from ∼62 $\mathrm{cm^{-1}}$ in $\mathrm{Bi_2Se_3}$ to ∼50 $\mathrm{cm^{-1}}$ in $T\mathrm{Bi_2Se_4}$, while the high-frequency A_{1g} is shifted from ∼135 $\mathrm{cm^{-1}}$ for $\mathrm{Bi_2Te_3}$ to ∼140 $\mathrm{cm^{-1}}$ for $T\mathrm{Bi_2Te_4}$. Contrary to this, the E_g modes are almost unchanged. As we mentioned previously, A_{1g} and E_g modes realize the out-of-plane and in-plane vibrations, respectively [43], and thus the distance between Te–Bi plays a crucial role [45]. Because the covalent interactions are much stronger along Te(1)–Bi–Te(2) than between Te–Te and Bi–Bi pairs, only the A_{1g} mode is shifted.

V. CIRCULAR PHONON POLARIZATION

The helicity of incident photons is completely reversed in the Raman process involving the doubly degenerate E_g

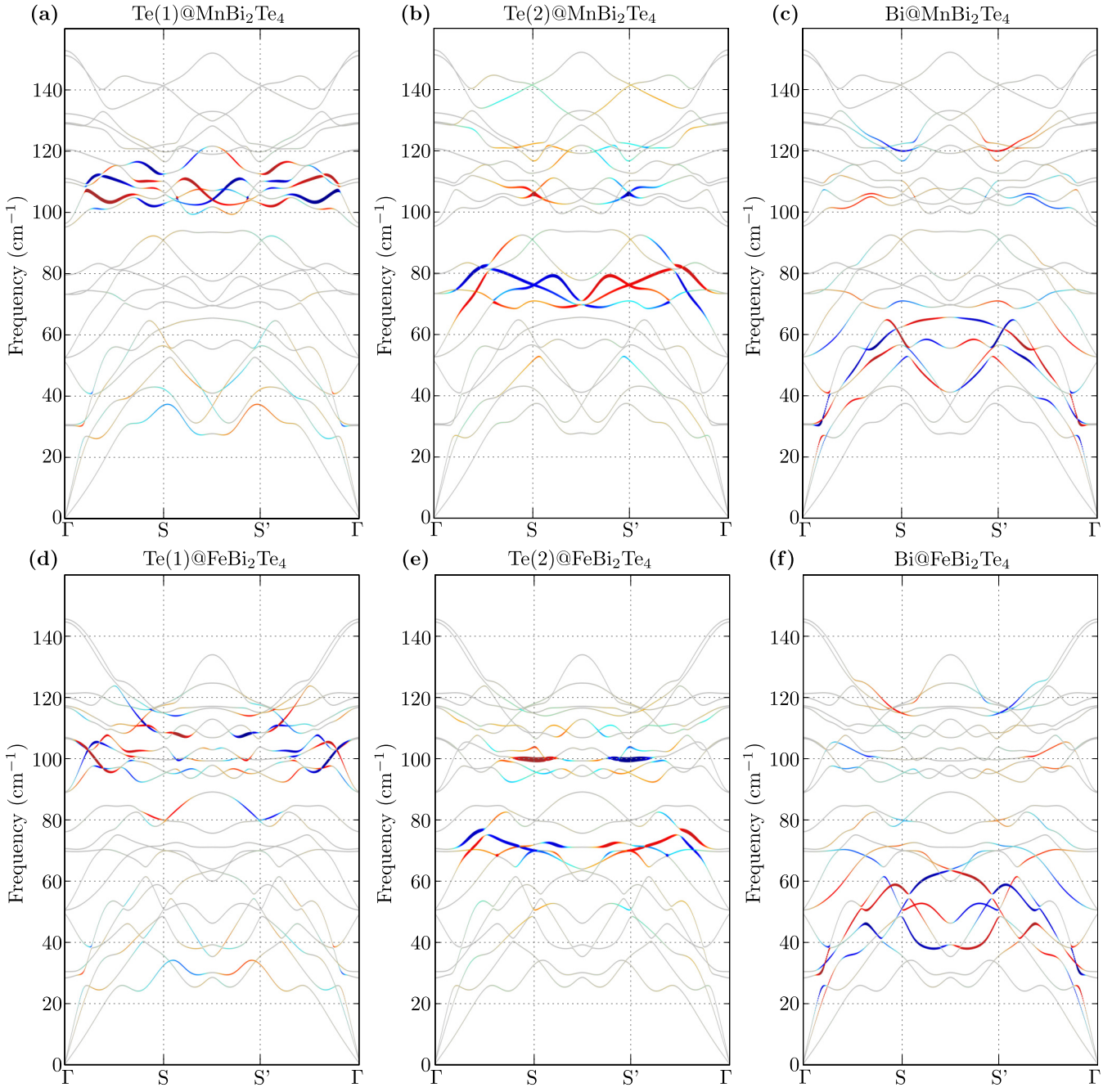

FIG. 4. Circular polarization of Te(1), Te(2), and Bi (panels from left to right) for $MnBi_2Te_4$ and $FeBi_2Te_4$ (top and bottom panels, respectively). Red and blue lines denotes left- and right-handed circular polarization of phonons, while the line width corresponds to the circulation value.

modes. This phenomenon is highly relevant in the context of circularly polarized phonons [54–58]. Indeed, $T\mathrm{Bi}_2\mathrm{Te}_4$ possesses the C_{3v} symmetry (each layer of atoms inside the SL forms a triangular lattice), which allows for the emergence of circularly polarized phonons [59]. Although none of the modes at the Γ point have the intrinsic chirality, we can obtain the chiral phonons via superimposing the doubly degenerate E_g modes [60]. Nevertheless, the chiral phonons can emerge out of the center of the Brillouin zone (i.e., away from the Γ point), where the degeneracy is lifted.

The circular polarization of the phonons can be studied by analyzing the phonon polarization vector, which can be found from the diagonalization of the dynamical matrix

$$D^{jj'}_{\alpha\beta}(\boldsymbol{q}) \equiv \frac{1}{\sqrt{m_j m_{j'}}} \sum_n \Phi_{\alpha\beta}(j0,\, j'n) \exp\left(i\boldsymbol{q}\cdot\boldsymbol{R}_{j'n}\right), \quad (3)$$

where $\boldsymbol{q}$ is the phonon wave vector and m_j denotes the mass of the jth atom. Here $\Phi_{\alpha\beta}(j0,\, j'n)$ is the IFC tensor (α and β denotes the direction index, i.e., x, y, and z) between the jth and j'th atoms located in the initial (0) and nth primitive unit cell. Then, the phonon spectrum as well as the polarization

vectors are given by the eigenproblem of the dynamical matrix

$$\omega^2_{\varepsilon \boldsymbol{q}} e_{\varepsilon \boldsymbol{q} \alpha j} = \sum_{j'\beta} D^{jj'}_{\alpha\beta}(\boldsymbol{q}) e_{\varepsilon \boldsymbol{q} \beta j'}. \tag{4}$$

Here, the ε branch describes the phonon with a frequency $\omega_{\varepsilon \boldsymbol{q}}$ and a polarization vector $e_{\varepsilon \boldsymbol{q} \alpha j}$. Each αj component of the polarization vector is associated with the displacement of the jth atom in the αth direction.

The phonon mode related to the particular polarization vector $e_{\varepsilon \boldsymbol{q} \alpha j}$ can be discussed in the context of the circular polarization. For this purpose, we introduce a new basis defined as [56–58] $|R_1\rangle \equiv \frac{1}{\sqrt{2}}(1\ i\ 0 \cdots 0)^T$; $|L_1\rangle \equiv \frac{1}{\sqrt{2}}(1\ -i\ 0 \cdots 0)^T$; $|Z_1\rangle \equiv \frac{1}{\sqrt{2}}(0\ 0\ 1 \cdots 0)^T$; $\cdots$; $|R_j\rangle \equiv \frac{1}{\sqrt{2}}(\cdots 1\ i\ 0 \cdots 0)^T$; $|L_j\rangle \equiv \frac{1}{\sqrt{2}}(\cdots 1\ -i\ 0 \cdots 0)^T$; $|Z_j\rangle \equiv \frac{1}{\sqrt{2}}(\cdots 0\ 0\ 1 \cdots 0)^T$; $\cdots$. It means that two in-plane components are replaced by the circular polarization vectors $\sigma^{\pm}$ (defined in Sec. IV), while the third component is unchanged. In this basis, each polarization vector $e \equiv e_{\varepsilon \boldsymbol{q} \alpha j}$, is represented as

$$e = \sum_j \left(\alpha^R_j |R_j\rangle + \alpha^L_j |L_j\rangle + \alpha^Z_j |Z_j\rangle\right), \tag{5}$$

where $\alpha^V_j = \langle V_j | e \rangle$, for $V \in \{R, L, Z\}$ and $j \in \{1, 2, \ldots, N\}$ (N is a total number of atoms in a primitive unit cell). The way of the jth atom movement is determined by a circulation $\mathcal{C} = |\alpha^R_j|^2 - |\alpha^L_j|^2$. When $\mathcal{C} = 0$, the atom is involved in an ordinary noncircular vibration, and when $\mathcal{C} \neq 0$, it realizes a circular motion.

In $T\mathrm{Bi_2Te_4}$, T atoms do not exhibit circular vibrations, being the only magnetic atoms in the compound. The other atoms, Te(1), Te(2), and Bi, realize a circular motion with different frequencies. Figure 4 presents a circular polarization of Te(1), Te(2), and Bi, along a path between two Γ points in the a-b plane (cf. Fig. 1). As the system possesses the inversion symmetry, atoms from opposite sites of the SL layer have an opposite circulation (i.e., the total circulation of the system is zero). The chiral phonons of Te(1), Te(2), and Bi are located around 110 cm^{-1}, 75 cm^{-1}, and 50 cm^{-1}. This "separation" of different types of phonons generating a circular motion of atoms is in agreement with the discussion of the phonon density of states (cf. Sec. III).

Let us briefly summarize this part. The emergence of chiral phonon modes is possible in described compounds due to the existence of the three-fold rotational symmetry [59]. Additionally, the presence of the inversion symmetry, leads to the vanishing of the total pseudoangular momentum of phonons [54]. The realization of the A-type AFM order in $T\mathrm{Bi_2Te_4}$ does not change the crystal symmetry so it has no direct effect on the chiral properties of phonons. The chirality of the system can be changed due to the crystal symmetry modifications induced by the external conditions [58,61], for example, the chiral modes can be efficiently manipulated by modifying the imposed strain. Similarly, the phase transition from the hexagonal to the orthorhombic structure affects the chiral phonons [58,62]. Under this transformation, the phonon bands degeneracy is lifted, and in consequence the chiral phonons with nonzero angular momentum can emerge. This type of phonon engineering can be useful for the practical implementation of the chiral phonon modes, e.g., in the designing of novel phononic quantum devices, based on the propagation of chiral phonon modes [63,64].

VI. SUMMARY

In this paper, we investigated the dynamical properties of $T\mathrm{Bi_2Te_4}$ (T = Mn, Fe) compounds. Both systems crystallize in the $R\bar{3}m$ rhombohedral structure. The phonon dispersion relations, derived for the structure with the A-type AFM order, do not exhibit any imaginary frequencies and thus, both compounds are dynamically stable. We performed the analyses of the mode symmetries at the Γ point. The Raman and infrared active modes were calculated. The frequencies of the Raman-active modes are in agreement with previous theoretical and experimental results. We point out that the Raman backscattering using co- or cross-circular configuration can be useful in distinguishing the A_{1g} and E_g Raman-active mode. Additionally, we show that the initially doubly degenerate E_g modes (at the Γ point), give rise to the emergence of the circularly polarized modes away from the Γ point. Moreover, chiral phonon modes are separated in the frequency domain depending on the atomic layer within the septuple layer.

ACKNOWLEDGMENTS

Some figures in this work were rendered using VESTA [65]. This work was supported by the National Science Centre (NCN, Poland) under Projects No. 2018/31/N/ST3/01746 (A.K.), No. 2017/25/B/ST3/02586 (M.S.), and No. 2016/21/D/ST3/03385 (A.P.). In addition, A.P. appreciates funding in the frame of scholarship of the Minister of Science and Higher Education of Poland for outstanding young scientists (2019 edition, No. 818/STYP/14/2019).

[1] M. M. Otrokov, I. I. Klimovskikh, H. Bentmann, D. Estyunin, A. Zeugner, Z. S. Aliev, S. Gaß, A. U. B. Wolter, A. V. Koroleva, A. M. Shikin, M. Blanco-Rey, M. Hoffmann, I. P. Rusinov, A. Y. Vyazovskaya, S. V. Eremeev, Y. M. Koroteev, V. M. Kuznetsov, F. Freyse, J. Sánchez-Barriga, I. R. Amiraslanov *et al.*, Prediction and observation of an antiferromagnetic topological insulator, Nature (London) **576**, 416 (2019).

[2] Y. Gong, J. Guo, J. Li, K. Zhu, M. Liao, X. Liu, Q. Zhang, L. Gu, L. Tang, X. Feng, D. Zhang, W. Li, C. Song, L. Wang, P. Yu, X. Chen, Y. Wang, H. Yao, W. Duan, Y. Xu *et al.*, Experimental realization of an intrinsic magnetic topological insulator, Chinese Phys. Lett. **36**, 076801 (2019).

[3] J.-Q. Yan, Q. Zhang, T. Heitmann, Z. Huang, K. Y. Chen, J.-G. Cheng, W. Wu, D. Vaknin, B. C. Sales, and R. J. McQueeney, Crystal growth and magnetic structure of $\mathrm{MnBi_2Te_4}$, Phys. Rev. Materials **3**, 064202 (2019).

[4] L. Ding, C. Hu, F. Ye, E. Feng, N. Ni, and H. Cao, Crystal and magnetic structures of magnetic topological insulators $\mathrm{MnBi_2Te_4}$ and $\mathrm{MnBi_4Te_7}$, Phys. Rev. B **101**, 020412(R) (2020).

[5] H. Li, S. Liu, C. Liu, J. Zhang, Y. Xu, R. Yu, Y. Wu, Y. Zhang, and S. Fan, Antiferromagnetic topological insulator $MnBi_2Te_4$: Synthesis and magnetic properties, Phys. Chem. Chem. Phys. **22**, 556 (2020).

[6] Y. Deng, Y. Yu, M. Z. Shi, Z. Guo, Z. Xu, J. Wang, X. H. Chen, and Y. Zhang, Quantum anomalous hall effect in intrinsic magnetic topological insulator $MnBi_2Te_4$, Science **367**, 895 (2020).

[7] D. Ovchinnikov, X. Huang, Z. Lin, Z. Fei, J. Cai, T. Song, M. He, Q. Jiang, C. Wang, H. Li, Y. Wang, Y. Wu, D. Xiao, J.-H. Chu, J. Yan, C.-Z. Chang, Y.-T. Cui, and X. Xu, Intertwined topological and magnetic orders in atomically thin Chern insulator $MnBi_2Te_4$, Nano Lett. **21**, 2544 (2021).

[8] C. Liu, Y. Wang, H. Li, Y. Wu, Y. Li, J. Li, K. He, Y. Xu, J. Zhang, and Y. Wang, Robust axion insulator and Chern insulator phases in a two-dimensional antiferromagnetic topological insulator, Nat. Mater. **19**, 522 (2020).

[9] Y.-J. Hao, P. Liu, Y. Feng, X.-M. Ma, E. F. Schwier, M. Arita, S. Kumar, C. Hu, R. Lu, M. Zeng, Y. Wang, Z. Hao, H.-Y. Sun, K. Zhang, J. Mei, N. Ni, L. Wu, K. Shimada, C. Chen, Q. Liu *et al.*, Gapless Surface Dirac Cone in Antiferromagnetic Topological Insulator $MnBi_2Te_4$, Phys. Rev. X **9**, 041038 (2019).

[10] B. Chen, F. Fei, D. Zhang, B. Zhang, W. Liu, S. Zhang, P. Wang, B. Wei, Y. Zhang, Z. Zuo, J. Guo, Q. Liu, Z. Wang, X. Wu, J. Zong, X. Xie, W. Chen, Z. Sun, S. Wang, Y. Zhang *et al.*, Intrinsic magnetic topological insulator phases in the Sb doped $MnBi_2Te_4$ bulks and thin flakes, Nat. Commun. **10**, 4469 (2019).

[11] Y. J. Chen, L. X. Xu, J. H. Li, Y. W. Li, H. Y. Wang, C. F. Zhang, H. Li, Y. Wu, A. J. Liang, C. Chen, S. W. Jung, C. Cacho, Y. H. Mao, S. Liu, M. X. Wang, Y. F. Guo, Y. Xu, Z. K. Liu, L. X. Yang, and Y. L. Chen, Topological Electronic Structure and its Temperature Evolution in Antiferromagnetic Topological Insulator $MnBi_2Te_4$, Phys. Rev. X **9**, 041040 (2019).

[12] W. Ko, M. Kolmer, J. Yan, A. D. Pham, M. Fu, F. Lüpke, S. Okamoto, Z. Gai, P. Ganesh, and A.-P. Li, Realizing gapped surface states in the magnetic topological insulator $MnBi_{2-x}Sb_xTe_4$, Phys. Rev. B **102**, 115402 (2020).

[13] D. Nevola, H. X. Li, J.-Q. Yan, R. G. Moore, H.-N. Lee, H. Miao, and P. D. Johnson, Coexistence of Surface Ferromagnetism and a Gapless Topological State in $MnBi_2Te_4$, Phys. Rev. Lett. **125**, 117205 (2020).

[14] A. M. Shikin, D. A. Estyunin, I. I. Klimovskikh, S. O. Filnov, E. F. Schwier, S. Kumar, K. Miyamoto, T. Okuda, A. Kimura, K. Kuroda, K. Yaji, S. Shin, Y. Takeda, Y. Saitoh, Z. S. Aliev, N. T. Mamedov, I. R. Amiraslanov, M. B. Babanly, M. M. Otrokov, S. V. Eremeev *et al.*, Nature of the Dirac gap modulation and surface magnetic interaction in axion antiferromagnetic topological insulator $MnBi_2Te_4$, Sci. Rep. **10**, 13226 (2020).

[15] A. M. Shikin, D. A. Estyunin, N. L. Zaitsev, D. Glazkova, I. I. Klimovskikh, S. O. Filnov, A. G. Rybkin, E. F. Schwier, S. Kumar, A. Kimura, N. Mamedov, Z. Aliev, M. B. Babanly, K. Kokh, O. E. Tereshchenko, M. M. Otrokov, E. V. Chulkov, K. A. Zvezdin, and A. K. Zvezdin, Sample-dependent dirac-point gap in $MnBi_2Te_4$ and its response to applied surface charge: A combined photoemission and ab initio study, Phys. Rev. B **104**, 115168 (2021).

[16] X.-M. Ma, Y. Zhao, K. Zhang, S. Kumar, R. Lu, J. Li, Q. Yao, J. Shao, F. Hou, X. Wu, M. Zeng, Y.-J. Hao, Z. Hao, Y. Wang, X.-R. Liu, H. Shen, H. Sun, J. Mei, K. Miyamoto, T. Okuda *et al.*, Realization of a tunable surface Dirac gap in Sb-doped $MnBi_2Te_4$, Phys. Rev. B **103**, L121112 (2021).

[17] J. A. Sobota, S.-L. Yang, D. Leuenberger, A. F. Kemper, J. G. Analytis, I. R. Fisher, P. S. Kirchmann, T. P. Devereaux, and Z.-X. Shen, Distinguishing Bulk and Surface Electron-Phonon Coupling in the Topological Insulator Bi_2Se_3 Using Time-Resolved Photoemission Spectroscopy, Phys. Rev. Lett. **113**, 157401 (2014).

[18] R. Heid, I. Y. Sklyadneva, and E. V. Chulkov, Electron-phonon coupling in topological surface states: The role of polar optical modes, Sci. Rep. **7**, 1095 (2017).

[19] G. Benedek, S. Miret-Artés, J. R. Manson, A. Ruckhofer, W. E. Ernst, and A. Tamtögl, Origin of the electron–phonon interaction of topological semimetal surfaces measured with helium atom scattering, J. Phys. Chem. Lett. **11**, 1927 (2020).

[20] A. Saxena, P. Rani, V. Nagpal, S. Patnaik, I. Felner, and V. P. S. Awana, Crystal growth and characterization of possible new magnetic topological insulators $FeBi_2Te_4$, J. Supercond. Nov. Magn. **33**, 2251 (2020).

[21] P. E. Blöchl, Projector augmented-wave method, Phys. Rev. B **50**, 17953 (1994).

[22] G. Kresse and J. Hafner, Ab initio molecular-dynamics simulation of the liquid-metal–amorphous-semiconductor transition in germanium, Phys. Rev. B **49**, 14251 (1994).

[23] G. Kresse and J. Furthmüller, Efficient iterative schemes for ab initio total-energy calculations using a plane-wave basis set, Phys. Rev. B **54**, 11169 (1996).

[24] G. Kresse and D. Joubert, From ultrasoft pseudopotentials to the projector augmented-wave method, Phys. Rev. B **59**, 1758 (1999).

[25] J. P. Perdew, K. Burke, and M. Ernzerhof, Generalized Gradient Approximation Made Simple, Phys. Rev. Lett. **77**, 3865 (1996).

[26] A. I. Liechtenstein, V. I. Anisimov, and J. Zaanen, Density-functional theory and strong interactions: Orbital ordering in Mott-Hubbard insulators, Phys. Rev. B **52**, R5467(R) (1995).

[27] C. Hu, K. N. Gordon, P. Liu, J. Liu, X. Zhou, P. Hao, D. Narayan, E. Emmanouilidou, H. Sun, Y. Liu, H. Brawer, A. P. Ramirez, L. Ding, H. Cao, Q. Liu, D. Dessau, and N. Ni, A van der Waals antiferromagnetic topological insulator with weak interlayer magnetic coupling, Nat. Commun. **11**, 97 (2020).

[28] S. Grimme, Semiempirical GGA-type density functional constructed with a long-range dispersion correction, J. Comput. Chem. **27**, 1787 (2006).

[29] H. J. Monkhorst and J. D. Pack, Special points for Brillouin-zone integrations, Phys. Rev. B **13**, 5188 (1976).

[30] H. T. Stokes and D. M. Hatch, FINDSYM: program for identifying the space-group symmetry of a crystal, J. Appl. Cryst. **38**, 237 (2005).

[31] A. Togo and I. Tanaka, SPGLIB: A software library for crystal symmetry search, arXiv:1808.01590.

[32] Y. Hinuma, G. Pizzi, Y. Kumagai, F. Oba, and I. Tanaka, Band structure diagram paths based on crystallography, Comput. Mater. Sci. **128**, 140 (2017).

[33] K. Parlinski, Z. Q. Li, and Y. Kawazoe, First-principles Determination of the Soft Mode in Cubic ZrO_2, Phys. Rev. Lett. **78**, 4063 (1997).

[34] T. Tadano, Y. Gohda, and S. Tsuneyuki, Anharmonic force constants extracted from first-principles molecular dynamics:

applications to heat transfer simulations, J. Phys.: Condens. Matter **26**, 225402 (2014).
[35] K. Parlinski, *Software PHONON*, Cracow (2019).
[36] Z. S. Aliev, I. R. Amiraslanov, D. I. Nasonova, A. V. Shevelkov, N. A. Abdullayev, Z. A. Jahangirli, E. N. Orujlu, M. M. Otrokov, N. T. Mamedov, M. B. Babanly, and E. V. Chulkov, Novel ternary layered manganese bismuth tellurides of the MnTe–Bi_2Te_3 system: Synthesis and crystal structure, J. Alloys Compd. **789**, 443 (2019).
[37] Y. Liu, X. Chen, and Y. Xu, Topological phononics: From fundamental models to real materials, Adv. Funct. Mater. **30**, 1904784 (2020).
[38] E. Aytan, B. Debnath, F. Kargar, Y. Barlas, M. M. Lacerda, J. X. Li, R. K. Lake, J. Shi, and A. A. Balandin, Spin-phonon coupling in antiferromagnetic nickel oxide, Appl. Phys. Lett. **111**, 252402 (2017).
[39] See Supplemental Material at http://link.aps.org/supplemental/10.1103/PhysRevB.105.214304 for the additional results of the phonon calculations performed using the magnetic unit cell.
[40] Y. Han, S. Sun, S. Qi, X. Xu, and Z. Qiao, Interlayer ferromagnetism and high-temperature quantum anomalous Hall effect in *p*-doped $MnBi_2Te_4$ multilayers, Phys. Rev. B **103**, 245403 (2021).
[41] R. Loudon, The Raman effect in crystals, Adv. Phys. **50**, 813 (2001).
[42] Y. Cho, J. H. Kang, L. Liang, X. Kong, S. Ghosh, F. Kargar, C. Hu, A. A. Balandin, A. A. Puretzky, N. Ni, and C. W. Wong, Phonon modes and Raman signatures of $MnBi_{2n}Te_{3n+1}$ ($n = 1, 2, 3, 4$) magnetic topological heterostructures, arXiv:2107.03204.
[43] M. Rodriguez-Vega, A. Leonardo, and G. A. Fiete, Group theory study of the vibrational modes and magnetic order in the topological antiferromagnet $MnBi_2Te_4$, Phys. Rev. B **102**, 104102 (2020).
[44] C. Pei, Y. Xia, J. Wu, Y. Zhao, L. Gao, T. Ying, B. Gao, N. Li, W. Yang, D. Zhang, H. Gou, Y. Chen, H. Hosono, G. Li, and Y. Qi, Pressure-induced topological and structural phase transitions in an antiferromagnetic topological insulator, Chinese Phys. Lett. **37**, 066401 (2020).
[45] P. Mal, G. Bera, G. R. Turpu, S. K. Srivastava, A. Gangan, B. Chakraborty, B. Das, and P. Das, Vibrational spectra of $Pb_2Bi_2Te_3$, $PbBi_2Te_4$, and $PbBi_4Te_7$ topological insulators: temperature-dependent Raman and theoretical insights from DFT simulations, Phys. Chem. Chem. Phys. **21**, 15030 (2019).
[46] N. K. Singh, D. Rawat, D. Dey, A. Elsukova, P. O. A. Persson, P. Eklund, A. Taraphder, and A. Soni, Electron-phonon coupling and quantum correction to topological magnetoconductivity in Bi_2GeTe_4, Phys. Rev. B **105**, 045134 (2022).
[47] J. Choe, D. Lujan, M. Rodriguez-Vega, Z. Ye, A. Leonardo, J. Quan, T. N. Nunley, L.-J. Chang, S.-F. Lee, J. Yan, G. A. Fiete, R. He, and X. Li, Electron–phonon and spin–lattice coupling in atomically thin layers of $MnBi_2Te_4$, Nano Lett. **21**, 6139 (2021).
[48] W. Richter and C. R. Becker, A Raman and far-infrared investigation of phonons in the rhombohedral V_2-VI_3 compounds Bi_2Te_3, Bi_2Se_3, Sb_2Te_3 and $Bi_2(Te_{1-x}Se_x)_3$ ($0 < x < 1$), $(Bi_{1-y}Sb_y)_2Te_3$ ($0 < y < 1$), Phys. Status Solidi B **84**, 619 (1977).
[49] V. Chis, I. Y. Sklyadneva, K. A. Kokh, V. A. Volodin, O. E. Tereshchenko, and E. V. Chulkov, Vibrations in binary and ternary topological insulators: First-principles calculations and Raman spectroscopy measurements, Phys. Rev. B **86**, 174304 (2012).
[50] L. Goncalves, C. Couto, P. Alpuim, A. Rolo, F. Völklein, and J. Correia, Optimization of thermoelectric properties on Bi_2Te_3 thin films deposited by thermal co-evaporation, Thin Solid Films **518**, 2816 (2010).
[51] K. M. F. Shahil, M. Z. Hossain, D. Teweldebrhan, and A. A. Balandin, Crystal symmetry breaking in few-quintuple Bi_2Te_3 films: Applications in nanometrology of topological insulators, Appl. Phys. Lett. **96**, 153103 (2010).
[52] B.-T. Wang and P. Zhang, Phonon spectrum and bonding properties of Bi_2Se_3: Role of strong spin-orbit interaction, Appl. Phys. Lett. **100**, 082109 (2012).
[53] J. O. Jenkins, J. A. Rayne, and R. W. Ure, Elastic moduli and phonon properties of Bi_2Te_3, Phys. Rev. B **5**, 3171 (1972).
[54] L. Zhang and Q. Niu, Angular Momentum of Phonons and the Einstein–de Haas Effect, Phys. Rev. Lett. **112**, 085503 (2014).
[55] Y. Liu, C.-S. Lian, Y. Li, Y. Xu, and W. Duan, Pseudospins and Topological Effects of Phonons in a Kekulé Lattice, Phys. Rev. Lett. **119**, 255901 (2017).
[56] L. Zhang and Q. Niu, Chiral Phonons at High-Symmetry Points in Monolayer Hexagonal Lattices, Phys. Rev. Lett. **115**, 115502 (2015).
[57] H. Chen, W. Wu, S. A. Yang, X. Li, and L. Zhang, Chiral phonons in kagome lattices, Phys. Rev. B **100**, 094303 (2019).
[58] A. Ptok, A. Kobiałka, M. Sternik, J. Łażewski, P. T. Jochym, A. M. Oleś, S. Stankov, and P. Piekarz, Chiral phonons in the honeycomb sublattice of layered CoSn-like compounds, Phys. Rev. B **104**, 054305 (2021).
[59] S. Coh, Classification of materials with phonon angular momentum and microscopic origin of angular momentum, arXiv:1911.05064.
[60] H. Chen, W. Zhang, Q. Niu, and L. Zhang, Chiral phonons in two-dimensional materials, 2D Mater. **6**, 012002 (2018).
[61] H. Rostami, F. Guinea, and E. Cappelluti, Strain-driven chiral phonons in two-dimensional hexagonal materials, Phys. Rev. B **105**, 195431 (2022).
[62] S. Basak and A. Ptok, Ab initio study of chiral phonons in ternary YAlSi compound, Crystals **12**, 436 (2022).
[63] H. Chen, W. Wu, J. Zhu, S. A. Yang, and L. Zhang, Propagating chiral phonons in three-dimensional materials, Nano Lett. **21**, 3060 (2021).
[64] J. Skórka, K. J. Kapcia, P. T. Jochym, and A. Ptok, Chiral phonons in binary compounds *A*Bi (A = K, Rb, Cs) with $P2_1/c$ structure, arXiv:2203.05524.
[65] K. Momma and F. Izumi, VESTA3 for three-dimensional visualization of crystal, volumetric and morphology data, J. Appl. Crystallogr. **44**, 1272 (2011).